PAPER

Check for updates

Empowering agriculture: rapid on-site soil nutrient detection with microfluidic colorimetry

Piyush Mishra, [ab] Priyanshi Gupta,[a] Sadhak Khanna, [ab] Bhupendra Pratap Singh, [c] Pallavi Mishra,[d] Swapnil Srivastava,[a] Sapna Yadav,[a] Sneha Kadian,[a] Shug-June Hwang [c] and Ved Varun Agrawal [*a]

This study introduces a novel methodology for the microfluidic colorimetric detection of soil analytes, offering enhanced efficiency for assessing plant growth parameters. Microfluidic channels (µPADs) were fabricated on paper substrates using a customized XY-Plotter equipped with a technical drawing pen containing an optimized polydimethylsiloxane (PDMS)-hexane solution, imparting hydrophobic properties to the substrate. The developed µPADs enabled visual detection of zinc concentrations ranging from 1 mg dL^{-1} to 45 mg dL^{-1} and orthophosphate concentrations from 0.5 g dL^{-1} to 8 g dL^{-1} in artificial soil (Hoagland's solution) through the formation of distinct colorimetric complexes. The calculated limits of detection (LOD) for zinc and orthophosphate were 0.0107 g dL^{-1} and 1.24 g dL^{-1}, while the limits of quantification (LOQ) were determined as 0.035 g dL^{-1} and 4.1 g dL^{-1}, respectively. The approach demonstrated high selectivity and sensitivity, providing rapid and reliable insights into the soil's nutrient profile. Compared to conventional methods, this innovative sensing platform is faster, cost-effective, and well-suited for on-site analysis of soil micro- and macronutrients. This advancement holds significant potential for agricultural practitioners, enabling informed decision-making to optimize soil fertility and support sustainable agricultural practices.

1. Introduction

The use of paper as a substrate material for analytical testing dates back to the early 1800s with the introduction of litmus paper. Paper-based sensing offers several unique advantages over traditional devices,[1] including low cost, flexibility, portability, fluid flow *via* capillary action without external power, a high surface area-to-volume ratio for colorimetric detection, and the ability to store reagents in an active form within its fibre network. These features make paper an invaluable material for analytical testing. The pioneering work of George M. Whiteside's group has significantly advanced the field of paper-based sensing technologies. The first paper-based microfluidic sensor, known as a microfluidic paper-based analytical device (µPAD), was introduced by Martinez *et al.* in 2007.[2] Their research demonstrated portable, low-cost bioassays on paper substrates patterned by photolithography.[3,4] Since then, various methods for creating paper µPADs have been developed[5],

including wax printing,[6,7] folded paper masks,[8–10] stamp lithography,[11,12] screen printing,[13,14] inkjet printing,[15,16] vapor phase deposition,[17–19] laser-toner printing,[20,21] 3D printing[22,23] and XY plotting. These methods have become standard for designing hydrophobic microfluidic channels on paper, providing low-cost, portable, and flexible diagnostic platforms.

Paper-based microfluidic devices are used for a wide range of sensing applications, including enzymatic, colorimetric, fluorescence detection mechanisms, and electrochemistry.[19,24–26] They have been employed in various biosensing applications, such as the colorimetric detection of phenolic compounds,[26–28] pathogen detection,[29,30] food safety and environmental monitoring,[31,32] immunoassay development,[33,34] and DNA and biochemical sensing.[35,36] These devices have also been used for tuberculosis detection using colorimetric gold nanoparticles.[37] Chiang *et al.*, in 2018[6] discussed the utilization of 3D wax-printed paper-based microfluidic barriers for glucose and nitrite assays. Another approach for patterning microfluidic channels in µPADs is described in the work of Lin *et al.*, 2020 which focuses on low-cost techniques based on polyurethane acrylate (PUA).[38,39] In this method, Whatman Grade 1 filter paper serves as the substrate, and water-based PUA is used to pattern the microfluidic channels. The process involves masking designed patterns on PUA-coated paper and exposing them to UV light[39] for curing. Similarly, in 2022 they have applied these techniques to pattern nitrocellulose membrane

[a] *CSIR-National Physical Laboratory, Dr K.S. Krishnan Marg, New Delhi-110012, India. E-mail: vedvarun@nplindia.org*

[b] *Academy of Scientific and Innovative Research (AcSIR), Ghaziabad-201002, India*

[c] *Department of Electro-Optical Engineering, National United University, Miao-Li-360, Taiwan*

[d] *Veer Bahadur Singh Purvanchal University, Jaunpur, Uttar Pradesh-222003, India*

papers for designing enzyme-linked paper-based immunosorbent assays.[38] However, it's important to note that this method relies on conventional lithographic techniques, particularly mask-based lithography. One limitation of mask-based lithography is that each mask is designed for a specific pattern of μPADs. While modifications in printed ink can enable detection of different analytes using the same design, changing the mask pattern itself is necessary when a design alteration is required, which adds complexity and cost to the fabrication process. The field of 3D printed microfluidic channels is rapidly evolving, offering significant advantages such as enhanced user-friendliness and versatility. Puneeth et al. conducted a comprehensive study focusing on optimizing and developing 3D printed μPADs for sensing applications. Their research incorporated an image processing mechanism to precisely measure the viscosity of biological samples, showcasing the potential of 3D printing in advancing microfluidic technology for analytical purposes.[40,41] The study by Zargaryan et al.[42] explores the use of polypropylene filament for creating 3D printed paper microfluidic channels. These channels are cured for at least 45 minutes at 175 °C. Although the channels are effective for point-of-care applications, the design process is complex, and the curing time is relatively long.

In previous work, we explored the fabrication of μPADs on various paper substrates using a DIY 3D printer equipped with a syringe pump. This method proved to be cost-effective and rapid, enabling the production of multiple μPADs for the colorimetric sensing of biological drugs, including paracetamol, ciprofloxacin, aspirin, and salicylic acid.[43] Our recent study showcases modification of DIY 3D printer assembled with technical drawing pens to fabricate microfluidic channels for on-spot chromogenic creatinine detection.[44] While the modified 3D printer offers a robust platform for μPAD fabrication and immediate curing with a heated bed, XY plotters present a compelling alternative for microfluidic applications. XY plotters are more cost-efficient, portable, and versatile, allowing operation on different substrates with a less restricted printing area compared to the typically limited bed size of 3D printers. Additionally, the DIY XY plotter utilized in this work requires only Inkscape V 1.2 for system interfacing and directly plots patterns without the need for G-Code conversion, which is necessary in our DIY 3D printer approach.

For low-cost, point-of-care diagnostics, the use of an XY plotter offers a dynamic alternative to traditional 3D printing, overcoming many associated drawbacks. In this method, hydrophobic solutions are dispensed from pens to create hydrophobic channels on paper substrates. This technique offers several advantages, including cost-effective fabrication, ease of channel formation, reduced waste, and enhanced environmental friendliness. However, it is important to note that implementing this technology often requires substantial modifications to the equipment. Bruzewicz et al. utilized an XY plotter to deposit hydrophobic barriers using a PDMS solution, aiming to balance cost-effectiveness and efficiency.[45] However, this approach involves intricate steps in pen fabrication. In contrast, Gallibu et al.[46] employed permanent markers to create hydrophobic barriers, offering rapid and cost-effective fabrication but with reduced flexibility due to the inherent

hydrophobic nature of marker ink. These limitations are then addressed in the work of Ghaderinezhad et al. by introducing a more efficient and cost-effective method for μPAD fabrication using permanent markers.[47] Amin et al.[48] introduced a technique using an XY plotter with high-resolution technical drawing pens and commercially available water-based hydrophobic solutions, varying pen nib sizes for optimization. Recently, Diela et al. presented a pen-on-paper method for fabricating daisy-shaped paper-based analytical devices (PADs). This versatile and cost-efficient method utilizes hydrophobic marker pens to create fluidic patterns, facilitating rapid prototyping without additional fabrication steps. The PADs enabled multiplexed colorimetric assays for antioxidants in wines, leveraging smartphone image processing to analyze unique color patterns per sample.[49] Despite these advantages, challenges include the limited ink capacity of permanent markers, posing constraints on mass production, and reliance on relatively expensive commercial instruments.

Table 1 lists the comparative analysis of the traditional techniques involved for μPADs fabrication.

Here we present a DIY XY plotter utilized to create hydrophobic channels on a paper substrate using technical drawing pens for identification of zinc and orthophosphate in Hoagland's artificial soil solution. Zinc is a crucial micronutrient for plants, playing key roles in enzyme activation, protein synthesis, and growth regulation. Both deficiency and excess of zinc influences plant growth. Insufficient zinc supply impairs important physiological functions, resulting in symptoms such as interveinal chlorosis, stunted growth, bronzing of leaves, small and abnormally shaped leaves, and rosetting. Conversely, excessive zinc levels can lead to toxicity. Therefore, maintaining an adequate supply of zinc is essential for achieving cost-effective crop yields globally.[60] Phosphorus is the macronutrient essential for optimal plant growth, influencing plant physiological responses and enhancing tolerance to various abiotic stresses including heat, salinity, drought, waterlogging, elevated CO_2 levels, and heavy metal toxicity.[61] Monitoring phosphorus levels effectively is necessary for maintaining plant health and productivity.[62,63] Plants possess mechanisms to perceive and respond to variations in phosphorus levels through dedicated signaling pathways, modifications in root architecture, and adjustments in stomatal morphology.[64,65] By modifying their phosphorus metabolism, plants endure a range of abiotic stresses, with stomatal responses being particularly significant.[66,67] Understanding the mechanisms by which plants perceive and acclimate to phosphorus availability is fundamental for developing strategies to improve crop yield and resilience to stress. Phosphorus plays a pivotal role in various metabolic and physiological processes essential for plant growth, such as energy transduction, cell division, DNA synthesis, and the formation of phospholipids, primarily in the forms of phosphate (Pi) or Pi esters.[68] Low Pi levels in the soil adversely affects fruit production, vegetative growth quality, and root development, ultimately leading to decreased crop yields.[69]

This study introduces an innovative method for soil point of care detection of zinc and orthophosphate levels in Hoagland's

Table 1 Comparison of distinct traditional techniques of μPADs fabrication

Fabrication process	Equipment required	Materials required	Limitations	Ref.
Wax printing	Wax printers	Wax	Resolution constraints, thermal instability	6 and 7
Screen printing	Customized masks	Wax, hydrophobic materials	Screen preparation, requires stencil design, limited resolution	13 and 50
Lithography	UV Lamp	Photoresist, hydrophobic material	Resolution constraints, thermal effects, paper property alteration, fabrication complexity, optimization needed	51 and 52
Paper folding and stamps	Customized masks	Wax, hydrophobic material	Stamp preparation, material absorption, ink diffusion issues	8
Inkjet printing	Inkjet printers	Customized liquid ink	Variability in channel formation, drying time, process delay. Surface treatment	30 and 53
Vapour phase deposition	Customized reaction chamber	Multiple chemicals	Vapor phase polymerization, requires specialized setup. Patterning complexity, longer fabrication steps	54
Laser toner printing	Toner laser printer	Customized toner, dye	Toner adhesion issues, inconsistent barrier formation, fabrication complexity, multi-step processing required	20,55
3D Printing	3D printer, filament material	Polypropylene, wax, polycaprolactone (PCL)	Ink spreading, inconsistent barriers, flow control, variability issues	56 and 57
3D Printer assembled with syringe pump	3D printer, syringe pump	PDMS, Hexane	Requires optimization of the flow rate, high standard deviation of barrier width, viscosity, and printing speed	43
XY plotter with pen	XY plotter, pen	PDMS, Hexane	Printing resolution, limited precision	45
XY Plotter with permanent marker	XY Plotter, permanent marker	Commercially available hydrophobic permanent markers	Manual patterning, reproducibility issues. Solvent compatibility, potential ink dissolution, fabrication consistency, variability in barrier formation	46
Desktop digital craft plotter with technical drawing pen	Desktop plotter, technical drawing pen	Aqueous bio ink containing BSA and commercially available hydrophobic inks	Pen precision, limited resolution, ink spreading, uncontrolled flow	58
XY plotter with technical drawing pen	XY plotter, technical drawing pen	Alkyl ketene dimer (AKD)	Fabrication speed, manual process. Requires to convert the design structures into g-codes, hydrophobic barrier stability, potential degradation	59
Pen-plotter attached with permanent markers	Pen-plotter, commercially available permanent markers	Hydrophobic permanent markers	Fixed solution of hydrophobic ink, ink spreading, uncontrolled flow	47
Desktop pen plotter with technical pen	Desktop pen plotter, technical pen	Commercially available water-based hydrophobic solution	Prolonged curing time of fabricated μpads, requires optimization of the plotting speed, unmodified ink solution	48
XY plotter equipped with commercially available pens and markers	XY Plotter, commercially available pens and markers	Hydrophobic inks	Expensive commercial plotters often impose constraints on the selection of hydrophobic inks. Multiplexing challenges, cross-reactivity issues. Color stability, requires controlled conditions	49
XY plotter with technical drawing pen	XY plotter, technical drawing pen	PDMS, Hexane	Requires optimization of the plotting speed for the better resolution of μpads	Present work

artificial soil using chromogenic agents for visual colorimetric analysis using DIY XY plotter and technical drawing pens. Zinc is identified by its formation of a pink-colored complex with dithizone, while orthophosphate reacts with acidic ammonium molybdate to produce a blue molybdenum complex upon reduction with ascorbic acid. The integration of XY plotters enhances versatility in microfluidic applications, providing a portable and cost-efficient alternative for patterning micro-structures on various substrates, which complements the study's goals of advancing sustainable agricultural practices through precise nutrient monitoring. This approach supports timely interventions to optimize plant nutrition, thereby pro-moting improved crop health and productivity.

2. Reagents and instruments

The cellulose membrane based Whatman Grade-1 Filter paper of pore size 11 μm is procured from Central Drug House (P) Ltd (CDH) Chemicals, India. Polydimethylsiloxane (PDMS) is pur-chased from ACROS Organics, New Jersey, Belgium. N-Hexane is purchased from Sisco Research Laboratories (P) Ltd, Mum-bai. Silicone Elastomer Curing Agent, Sylgard 184 is acquired from Dow Corning Corporation Midland - Michigan U.S.A.

For the preparation of artificial soil, potassium nitrate (KNO_3), calcium nitrate tetrahydrate (Ca $(NO_3)_2 \cdot 4H_2O$), boric acid (H_3BO_3), EDTA ferric monosodium salt ($C_{10}H_{12}N_2O_8FeNa$) are purchased from CDH Chemicals, India. Manganese(II) chloride tetrahydrate purified ($MnCl_2 \cdot 4H_2O$) is procured from Merck Specialities Private Limited, Mumbai. Cupric Sulphate ($CuSO_4 \cdot 5H_2O$) is purchased from Qualigens Fine Chemicals, Mumbai. Ammonium molybdate (($NH_4)_6Mo_7O_{24} \cdot 4H_2O$) is procured from Thermo Fisher Scientific India Pvt. Ltd, Mumbai. For the colorimetric reactions, zinc sulfate heptahydrate purified ($ZnSO_4 \cdot 7H_2O$) is purchased from Merck Specialities Private Limited, Mum-bai. Dithizone AR Reagent ($C_{13}H_{12}N_4S$) is purchased from CDH Chemicals, India. Di-potassium hydrogen orthophosphate anhy-drous LR (K_2HPO_4) is acquired from s.d. Fine-Chem Ltd, Mumbai. L-Ascorbic acid ($C_6H_8O_6$) is obtained from Sigma Chemical CO, USA. The curing of the μPADs is done in KENSTAR OM-29ECF microwave oven. The contact angle measurements are carried out by the Dataphysics OCA 15 EC equipment. UV-vis spectroscopy is performed by SPECORD 210 Plus. The analysis of the scanned images are performed by using ImageJ 1.54j Wayne Rasband, Contributor National Institutes of Health, USA. SEM and EDAX analysis are done utilizing Tescan magna GMH and EDAX Octane elect. Super. All the images are captured using Samsung Galaxy M31 autofocus camera (f/1.8 aperture) fixed at 30 cm height from the substrate.

3. Fabrication of microfluidic paper based device (μPADS)

3.1. μPADs fabrication

A DIY XY plotter equipped with a technical drawing pen is employed for fabricating μPADs on Whatman Grade 1 paper substrate. This substrate consists of a cellulose-based
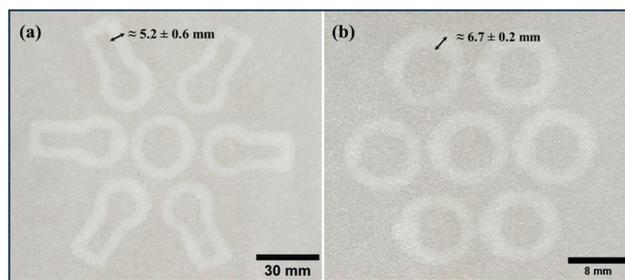

Fig. 1 Analysis of the width measurement in the prepared μPADs for (a) zinc and (b) orthophosphate colorimetric sensing.

membrane with a pore size of 11 μm. The plotter is interfaced with Inkscape V 1.2 open-source software, utilizing the AxiDraw extension as its controller. The printing speed is a critical parameter in μPAD fabrication as the high speeds causes micro pad breakage, while slower speeds result in wider features.[43] To maintain barrier uniformity, the pen speed is set at 8% (30.4 mm s^{-1}) in the AxiDraw settings. Fluid infusion is regulated using technical drawing pens. Polydimethylsiloxane (PDMS) is mixed with curing agent, Sylgard 184, in a 10:1 ratio. To optimize the viscosity of the PDMS and Sylgard mixture for smooth flow through the drawing pen, hexane is added at a 1:3 ratio. Specifically, 1 mL of hexane is mixed with every 3 mL of the PDMS and Sylgard blend. This solution is then loaded into a pen with a 0.6 mm nib diameter attached to the XY plotter. A schematic of the fabrication setup is shown in Fig. 1. Video file demonstrating the μPAD fabrication process is presented as supplementary. The curing temperature is optimized at 150 °C for 15 minutes using a microwave oven. Two μPADs are designed for colorimetric detection of zinc and orthophosphate (Fig. 1(a) and (b)). Evaluation of the fabricated μPADs involved analysis using ImageJ software. The measured mean width of the μPADs (Fig. 1(a)) is 5.2 mm, with a standard deviation of 0.6 mm. While of (Fig. 1(b)) is 6.7 mm, with a standard deviation of 0.2 mm as shown in the Fig. 1. The fabricated μPADs feature hydrophobic boundaries that confine the reagent and analyte flow, enabling analysis within these defined regions.

3.2. Contact angle measurements

The hydrophobic properties of Whatman Grade-1 paper treated with an optimized PDMS: Hexane solution have been charac-terized using contact angle analysis. This method facilitates in evaluating the hydrophobic nature of the microfluidic pads (μPADs), which directly impacts their performance in various applications. To ensure precise and consistent results, mea-surements are conducted at a constant temperature of 20 °C. This controlled environment allows for the observation of the temporal effects on the hydrophobicity of the PDMS channels over time. The contact angle is assessed following treatment of the paper with the optimized PDMS: Hexane solution and subsequent curing at 150 °C for 15 minutes. This curing step stabilizes the hydrophobic coating, ensuring consistent and reliable hydrophobic behavior of the μPADs. The mean contact angle, averaged over ten measurements shown in Fig. 2. is
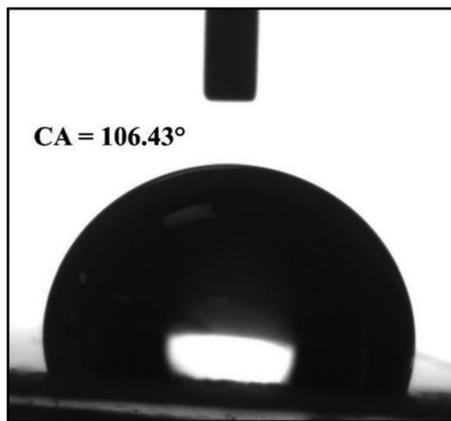
Fig. 2 Contact angle measurement on Whatman Grade-1 filter paper coated with the optimized hydrophobic solution of PDMS: hexane.

106.43°. This clearly indicates the entirely hydrophobic nature of the printed µPADs. This strong hydrophobic property validates their suitability for applications requiring rapid and sensitive detection capabilities, where prompt and accurate results are essential.

3.3. Scanning electron microscopy

Surface topography analysis is performed using SEM on both uncoated and PDMS-coated Whatman G1 filter papers at a resolution of 20 µm and magnification of 2000× (see Fig. 3(a) and (b)). The results indicate that the coating process reduces surface roughness and pore size, resulting in increased hydrophobicity of the paper. The energy dispersive X-ray analysis (EDAX) plots shown in Fig. 3(a′) and (b′) reveal a significant increase in silicon concentration on the PDMS-coated Whatman paper. Peaks for carbon and oxygen are attributed to the cellulose content of the paper, while the gold peak is due to the conductive gold coating applied for SEM analysis.

The observations from contact angle analysis and SEM offer critical insights into the hydrophobic properties of Whatman G1 filter papers prior to and following PDMS coating. This hydrophobic nature is essential for the fabrication of µPADs, ensuring effective fluid control.

4. Colorimetric analysis of the target analytes

4.1. Synthesis of artificial soil

The artificial soil is prepared according to the Hoagland methodology,[70,71] which involves the precise blending of essential macro and micronutrients required for optimal plant growth. Hoagland's solution is a standardized chemical formulation that comprehensively represents the nutritional requirements for plant cultivation. Detailed information
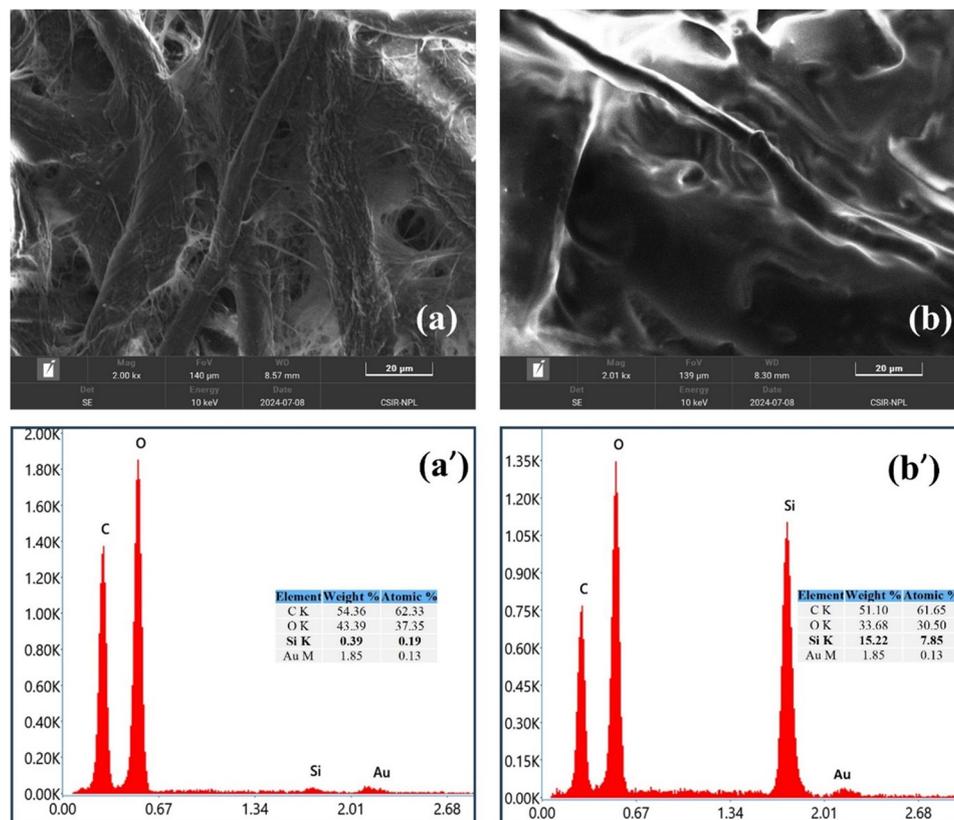

Fig. 3 Scanning electron microscopy (SEM) analysis on Whatman Grade-1 filter paper (a) uncoated and (b) coated with the optimized hydrophobic solution of PDMS: Hexane. (a′) and (b′) represent the EDAX response on the uncoated and coated paper substrates respectively.

Table 2 Chemicals and their concentration in DI for synthesis of artificial soil

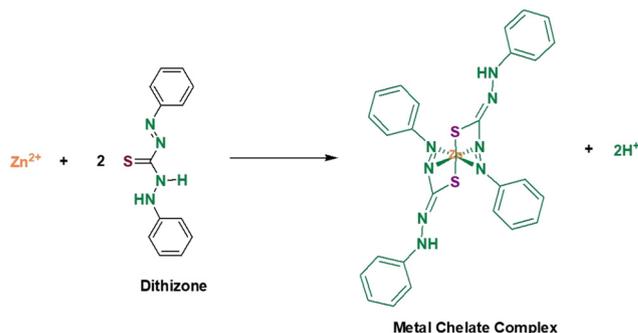| Chemicals used	Concentration (g/500 mL)
Potassium nitrate	41.05 g
Calcium nitrate tetrahydrate	59.04 g
Magnesium sulphate heptahydrate	30.8 g
Boric acid	0.142 g
Manganese chloride tetrahydrate	0.0495 g
Copper sulphate pentahydrate	0.025 g
Ammonium molybdate	0.618 g
EDTA ferric monosodium salt	8.2586 g

regarding the chemicals used and their respective concentrations in the formulation of the artificial soil is found in Table 2 provided.

Two distinct μPAD designs are utilized for the colorimetric sensing of zinc and orthophosphate, tailored to the specific reaction mechanisms and reagents involved. The capillary action-based colorimetric response for zinc is effective due to the involvement of a single reagent. Conversely, the detection of orthophosphate, which requires two reagents, benefits from on-spot color generation. Therefore, circular μPADs are advantageous for orthophosphate detection.

This study utilized an artificial soil solution in the analysis. Regarding real soil samples, preprocessing is required to prepare a solution suitable for colorimetric evaluation.[72]

4.2. Colorimetric detection of zinc

The typical concentration of zinc in agriculturally rich soils ranges from 10 to 300 μg per gram of soil.[73] Consequently, the corresponding zinc concentrations is estimated to range from 1 to 30 mg dL^{-1}, with density of a deionized water-based Hoagland solution 1 g mL^{-1}. Colorimetric detection of zinc on μPADs spanning concentrations from 1 mg dL^{-1} to 45 mg dL^{-1} involves the utilization of Dithizone solution. This solution is prepared by dissolving 0.04 g of Dithizone in 10 mL of methanol, yielding a dark blue-green solution upon agitation, which is subsequently filtered for consistency. Six test solutions are prepared containing varying concentrations of zinc (1 mg, 5 mg, 10 mg, 20 mg, 35 mg, 45 mg) per dL of artificial soil solution. The baseline zinc sulfate concentration in the artificial soil, prepared according to the Hoagland solution, is 2 mg per 10 mL, serving as the reference standard. To quantify zinc ions across these concentrations, a colorimetric method is employed. This method hinges on the formation of a pink-colored complex when Dithizone reacts with Zincate ions. Dithizone, or diphenylthiocarbazone, is a multi-dentate ligand with one sulfur and four nitrogen donor atoms, selectively forming coordination complexes with metal ions. In the presence of zinc ions, Dithizone undergoes coordination chemistry where its thione groups' sulfur atoms as well as nitrogen atoms act as ligands, donating electron pairs to zinc ions. This coordination results in the creation of a metal chelate complex characterized by a pink hue. The intensity of this pink complex directly correlates with the concentration of zinc ions in the artificial soil solutions. The reaction mechanism is depicted in Scheme 1.

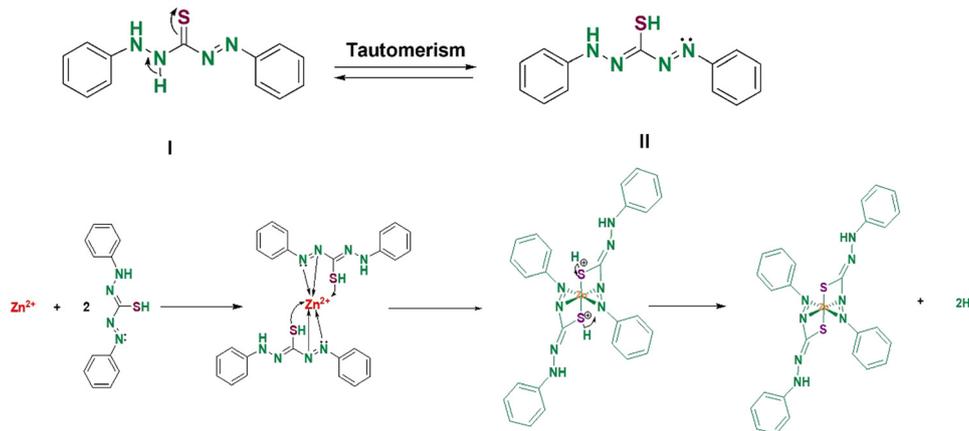**Scheme 1** Reaction of zincate ions with Dithizone forming a metal chelate complex.

Dithizone is a tri-dentate ligand which forms coordinate bonds with metal with its three donor atoms like N, N and S.[74] The octahedral geometry is more favorable than the tetrahedral geometry due to the CFSE being higher and sterically favourable. The structure I is first converted into structure II which forms co-ordinate bonds by transferring electrons from its donor atoms (N, N and S) to metal Zn^{2+} to form a octahedral complex and due to the presence of hydrogen on sulfur, it gets a positive charge which then gives off H^+ and forming neutral complex (Scheme 2).

The experimental procedure for naked-eye colorimetric detection of zinc involves dispensing a 2 μL drop of Dithizone onto the paper μPADs. The dispensed reagent is subsequently allowed to air-dry for 5 minutes, after which 1 μL of artificial soil solution is added. The solution with varying concentrations of zinc chemically reacts with the Dithizone resulting in visible pink coloration, attributed to the complex formation between Dithizone and zinc ions, exhibits a dependence on the concentration of zinc added, as shown in the Fig. 4(a). Image processing is performed to quantitatively analyze colorimetric detection by plotting a calibration curve with intensity versus concentration values. The linear relationship obtained in the graph indicates that as the concentration increases, the intensity of the formed color complex also increases. Images of the paper devices are scanned and saved in JPEG format at 300 dpi. The average gray intensity of color formation at the detection reservoirs is measured using ImageJ software. A color threshold was applied to each image by adjusting the hue to isolate the color of interest and removing any background contribution. Once optimized, the threshold ranges were fixed for each assay. After threshold adjustment, the images were converted to 8-bit grayscale and inverted so that darker colors yielded greater intensity. The program then automatically selected the regions of interest in the image using the Wand tool, and the average gray intensity was measured.[75] The relative dependency of intensity on concentration is shown in Fig. 4(b). The graph verified that as the concentration of the target analyte increases, the intensity of the colored complex formed also increases.

4.3. Colorimetric detection of orthophosphate

The standard concentration of orthophosphate, as defined by the Hoagland solution, is 0.43 g per 10 mL. In the context of

Scheme 2 Mechanism of Zn^{2+} with tridentate ligand (Dithizone) forming octahedral chelate complex.
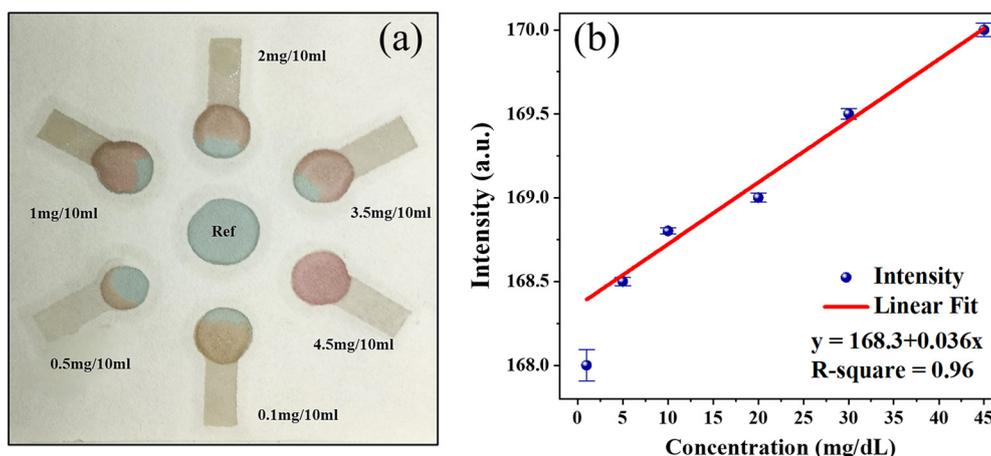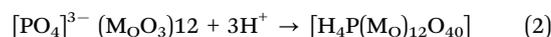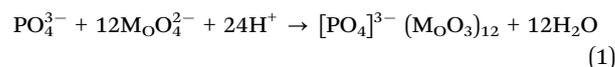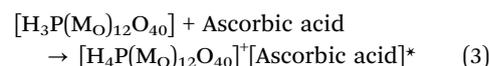

Fig. 4 (a) Concentration based colorimetric detection of zinc in artificial soil solutions on µPADs. (b) Quantitative Analysis studied by calibration curve generated for the range of 1 mg dL^{-1} to 45 mg dL^{-1} zinc by measuring the intensity of color formed in detection reservoirs.

soil, the typical phosphorus concentration ranges from 50 to 3000 mg kg^{-1}. This phosphorus primarily exists as orthophosphate, which is quantified as 5 to 300 mg dL^{-1} in Hoagland's solution.[76] The colorimetric reactions are performed over a wider concentration ranging from 0.5 g dL^{-1} to 8 g dL^{-1}. Six concentrations of orthophosphate including 0.5 g, 1.5 g, 3 g, 4 g, 6.5 g, and 8 g are prepared per dL of the Hoagland solution. The reagent is prepared by dissolving 1 g of ammonium molybdate in 25 mL deionized water (DI). To expedite the reaction rate, the ammonium molybdate solution is acidified by the addition of 200 µL of 11.45 M concentrated hydrochloric acid. Additionally, 0.25 g of Ascorbic is dissolved in 25 mL DI. The colorimetric experimental procedure involves two key steps, the addition of 1 µL ammonium molybdate solution, followed by the addition of 1 µL of solutions containing various concentrations of phosphate ions. Subsequently, 1 µL of ascorbic acid solution is added. This sequence results in the development of a blue color on the µPADs, with the intensity correlating directly with the levels of orthophosphate in the artificial soil as shown in Fig. 5(a). The intensity *vs.*

concentration plot shown in Fig. 5(b) correlates the dependency between these parameters. In this method, ammonium molybdate, under strong acidic conditions, reacts with orthophosphate according to eqn (1) and (2) forms Keggin ion.[77]

$$PO_4^{3-} + 12M_OO_4^{2-} + 24H^+ \rightarrow [PO_4]^{3-}(M_OO_3)_{12} + 12H_2O \tag{1}$$

$$[PO_4]^{3-}(M_OO_3)12 + 3H^+ \rightarrow [H_4P(M_O)_{12}O_{40}] \tag{2}$$

This intermediate is then reduced by ascorbic acid, as per eqn (3), yielding the molybdenum blue complex responsible for the blue coloration observed.

$$[H_3P(M_O)_{12}O_{40}] + \text{Ascorbic acid} \rightarrow [H_4P(M_O)_{12}O_{40}]^+[\text{Ascorbic acid}]^* \tag{3}$$

The negative charge of oxygen atom of ammonium molybdate, acting as a base abstracts H$^+$ ions from H$_2$SO$_4$ and molybdic acid is formed which then removes the water molecule to form molybdenum trioxide (Scheme 3).
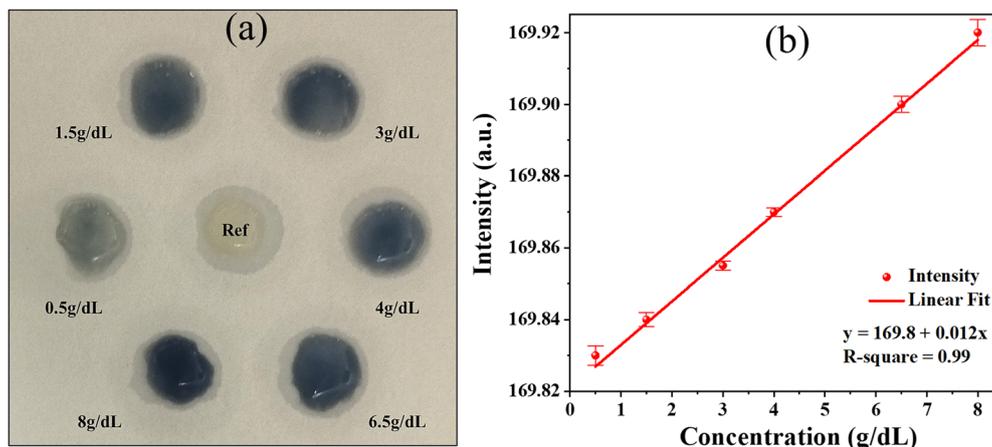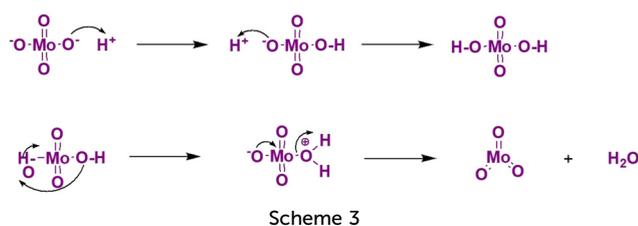
Fig. 5 (a) Concentration based colorimetric detection of orthophosphate in artificial soil solutions on paper µPADs. (b) Quantitative analysis studied by calibration curve generated for the range of 0.5–8 g dL^{-1} orthophosphate by measuring the intensity of color formed in detection reservoirs.

Scheme 3

The molybdenum trioxide (12 molecules) trap phosphate ion inside it's cavity formed, due to the interaction of opposite charges (positive of molybdenum and negative of oxygen atom of phosphate ion) which forms a cyclic complex in the presence of H$^+$ ions and blue colour positively charged complex is formed by the addition of ascorbic acid[78] (Scheme 4).

4.4. Kinetics study

In the context of colorimetric detection of target analytes, understanding the reaction kinetics between reagents and reactants is pivotal. To clarify the correlation between analyte concentration and reaction time, kinetic studies of these reactions were conducted. Our results demonstrate that the reaction rate escalates proportionally with analyte concentration, offering insights into the reaction's order. Through comprehensive analysis, we ascertain that the reaction adheres to first-order kinetics. Further elaboration, supported by detailed explanations and data illustrating first-order reaction kinetics, is presented in subsequent sections. A first-order reaction is defined as a chemical reaction in which the reaction rate is directly proportional to the concentration of a single reactant.[79] This means the rate of the reaction changes linearly with variations in the concentration of that reactant.

The differential rate law for the first order reaction kinetics is given as eqn (4).

$$\text{Rate} = -\frac{d[A]}{dt} = k[A] \tag{4}$$

where, (k) represents the rate constant and (A) is the concentration of the first-order reactant. The rate of change of concentration of (A) is given as $\frac{d[A]}{dt}$.

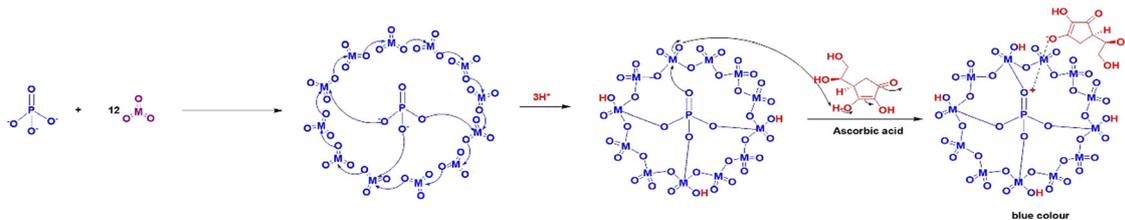The integrated rate law for the first order reaction is evaluated using eqn (5).

$$\ln[A] = -kt + \ln[A]_o \tag{5}$$

where k represents the slope of the equation.

4.4.1. Zinc. To determine the reaction order and kinetics, images were captured and subsequently analyzed using ImageJ software. It is observed that higher concentrations of zincate ions produced a darker pink complex when reacted with dithizone. This observation suggests a direct correlation between the color intensity and the concentration of zincate ions within the solutions of artificial soil. Fig. 6(a) shows the progressive development of the pink color over time, illustrating the temporal relationship with concentration. The integrated rate law for the kinetics of the first-order reaction is shown in Fig. 6(b).

The formation of the metal–chelate complex correlates directly with the intensity of the resulting color. Increasing concentrations of zincate ions correspond to accelerated reaction rates, leading to rapid complex formation at higher concentrations. Conversely, lower concentrations necessitate a longer reaction time on the prepared µPADs, highlighting the concentration-dependent nature of the reaction kinetics. At the highest concentration tested (45 mg dL^{-1}), the metal–chelate complex forms within 4 seconds, whereas at the lowest concentration (1 mg dL^{-1}), it requires 10 seconds. The development of pink coloration on the prepared µPADs facilitates real-time analysis of reaction kinetics, visually indicating the presence and concentration of zincate ions. This observation confirms a first-order reaction mechanism, where the reaction rate increases with higher concentrations of zincate ions. The linearity corresponds to the integrated rate law equation, with

Scheme 4 Mechanism of PO_4^{3-} with ammonium molybdate in presence of ascorbic acid, forming blue colour complex.
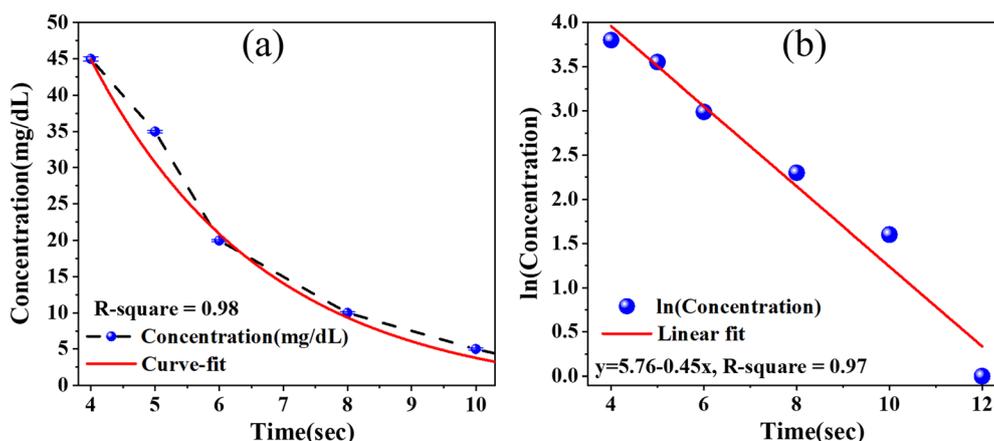

Fig. 6 Reaction kinetic study on prepared μPADs: (a) Formation of a pink-colored complex as a function of time, and (b) A linear relationship between ln (concentration) and time, indicating first-order reaction kinetics with a downward slope.

the slope of this line yielding the rate constant (k) of 0.45 s^{-1} (Fig. 6(b)).

4.4.2. Orthophosphate. The increment in the orthophosphate concentration accelerates the reaction rate, leading to rapid complex formation at higher concentrations compared to lower ones on the prepared μPADs. This concentration-dependent reaction rate is illustrated in Fig. 7, where Fig. 7(a) shows the time-dependent development of blue color, clearly depicting shorter reaction times at higher concentrations (8 g dL^{-1} within 10 seconds) compared to lower concentrations

(0.5 g dL^{-1} within 17 seconds). Visual detection of the blue color facilitates real-time analysis of reaction kinetics, confirming a first-order reaction kinetics where the rate law equation is represented in Fig. 7(b). The linear relationship observed in the graph enables determination of the rate constant (k), calculated as 0.38 s^{-1}.

For the kinetic study, images were captured using video analysis with the smartphone camera (mentioned in Section 1) positioned 30 cm from the samples. The video recordings facilitated precise timepoint identification, and each image
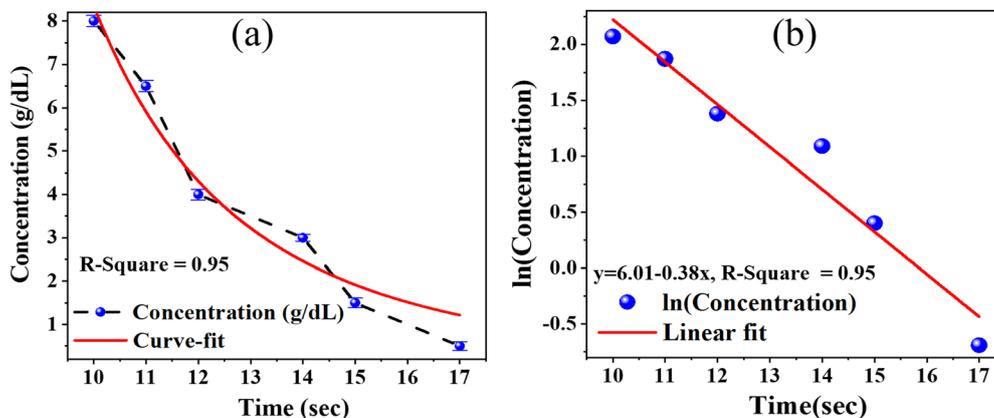

Fig. 7 Reaction kinetic study on prepared μPADs: (a) formation of a blue-molybdenum complex as a function of time, and (b) a linear relationship between ln (concentration) and time, indicating first-order reaction kinetics with a downward slope.
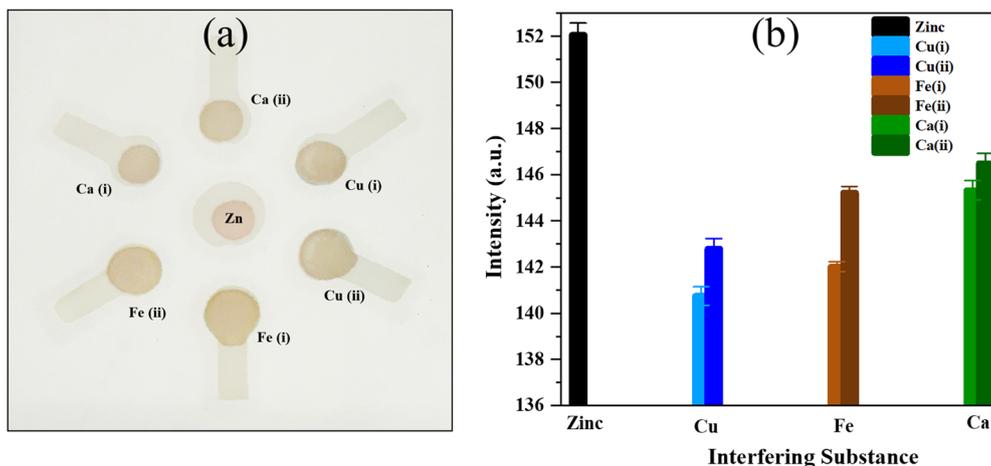
Fig. 8 Selectivity analysis of potentially interfering substances (a) on μPADs (b) correlation of the intensity of interfering substances.

was extracted from separate samples to ensure accuracy in the analysis.

5. Selectivity analysis

The selectivity analysis assesses the impact of potentially interfering substances in artificial soil on the detection of the target analytes, specifically zinc and orthophosphate. This analysis is crucial in determining the specificity of a chromogenic agent towards its intended target analyte. For zinc detection, the selectivity analysis evaluates the influence of various interfering substances, including copper ions, calcium ions, and iron. Each of these substances is tested to ascertain whether they affect the chromogenic reaction used for zinc detection. Similarly, for orthophosphate detection, iron is considered as a potential interfering substance.

By conducting these selectivity analyses separately for zinc and orthophosphate, this study enhances the reliability of the colorimetric detection method for accurately monitoring zinc and orthophosphate levels in artificial soil.

5.1. Zinc

The standard levels of potentially interfering substances in Hoagland's artificial soil are defined by specific concentrations: copper at 0.025 g/500 mL, Calcium at 59.04 g/500 mL, and iron at 8.25 g/500 mL. For the selectivity analysis, two elevated concentrations are considered for each interfering substance: Fe(I) (2.5 g dL^{-1}), Fe(II) (3 g dL^{-1}), Ca(I) (15 g dL^{-1}), Ca(II) (20 g dL^{-1}), Cu(I) (0.01 g dL^{-1}) and Cu(II) (0.015 g dL^{-1}), resulting in a total of six distinct solutions in artificial soil. These solutions are used to compare observations with the normal zinc concentration, set at 20 mg dL^{-1} or 0.02 g dL^{-1}. The experimental procedure involves applying 2 μL of Dithizone onto μPADs. Following this, 1 μL of each interfering substance is added, with zinc acting as the reference point at the center of the μPADs. (see Fig. 8(a)). The intensity of each potentially interfering substance is calculated from their respective RGB values. As shown in Fig. 8(b), a graph plotting

Table 3 Interference percentage of potentially interfering substances calculated from their respective intensity in artificial soil

Substance	Interference (%)
Fe(I)	−6.60
Fe(II)	−4.48
Ca(I)	−4.42
Ca(II)	−3.66
Cu(I)	−7.43
Cu(II)	−6.30

intensity against concentration concludes that even at elevated concentrations of potentially interfering substances, there is no evident colorimetric interference visible to the naked eye. The experiments were conducted five times, and the average values were used for statistical analysis. Hence, the study ensures that Dithizone reacts specifically with zinc without interference from other common soil constituents.

The assessed percentage interference values are evaluated employing eqn (6) and presented in the accompanying Table 3.

$$\% \text{ Interference} =$$

$$\left(\frac{\text{Intensity of interferring substance} - \text{Intensity of zinc}}{\text{Intensity of zinc}} \right) \times 100$$

$$(6)$$

The analysis derived from the Table 3 indicates that even at elevated concentrations, the presence of interfering substances exerts minimal interference.

5.2. Orthophosphate

The specificity of the reagents used for the orthophosphate color complex is assessed in the presence of elevated iron (Fe) concentrations, known to potentially interfere. The standard Fe concentration in Hoagland's artificial soil is 1.65 g per dL. To evaluate reagent selectivity, a higher Fe concentration of 3 g dL^{-1} is employed. Observations are compared with the normal orthophosphate level (4 g dL^{-1}) prepared in the artificial soil, as
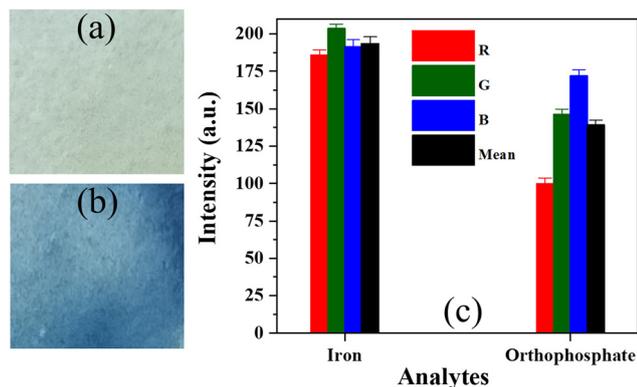
Fig. 9 Colorimetric observation on paper with ammonium molybdate and ascorbic acid of (a) iron and (b) orthophosphate (c) presents the histogram pot of RGB values for colorimetric observations on paper.

shown in Fig. 9(a) and (b). The experimental procedure begins with the application of 1 μL of ammonium molybdate onto μPADs, followed by separate additions of 1 μL of Fe solution and 1 μL of orthophosphate solution. Subsequently, 1 μL of ascorbic acid solution is introduced. Images are captured and analyzed using ImageJ software. Fig. 9(c) presents the plot of the intensity against concentration demonstrates distinct intensity values for Fe (3 g dL^{-1}) and orthophosphate (4 g dL^{-1}), indicating no visible colorimetric interference even at elevated Fe concentrations. The statistical analysis is performed for five repetitions. This study underscores the specific reaction of ammonium molybdate and ascorbic acid with orthophosphate, unaffected by other common soil constituents.

6. UV-vis spectroscopy

The analysis of colorimetric reactions using UV-vis spectroscopy allows for the spectrophotometric identification of complex formation within a specific wavelength range, indicative of particular electronic transitions associated with specific reactions. Additionally, a calibration curve generated between absorbance and concentration exhibits their linear relationship, facilitating the calculation of the LOD and LOQ values.

6.1. Zinc

The reaction between dithizone and zincate ions produces a pink-colored metal chelate complex. This coordination complex forms as a result of electron donation to the zincate ions, leading to a maximum absorbance wavelength λ_{max} of approximately 590 nm (Fig. 10(a)).[80] The transition occurring at this higher wavelength is indicative of a specific electronic transition associated with the complex. A calibration curve is constructed to illustrate the relationship between absorbance and the concentration of zincate ions (Fig. 10(b)). The statistical analysis is conducted based on five repeated measurements. The linear correlation observed in the range of 1 mg dL^{-1} to 45 mg dL^{-1} demonstrates that higher absorbance values are directly proportional to higher concentrations of zincate ions. This linear relationship confirms the sensitivity and reliability of the assay for quantifying zincate ion concentrations.

6.2. Orthophosphate

The blue-colored complex formed from the reaction between ammonium molybdate and ascorbic acid with orthophosphate exhibits a λ_{max} value of approximately 270 nm within the time duration of 1 minute (Fig. 11(a)). This peak is indicative of an electronic transition. Given that the λ_{max} value occurs at a shorter wavelength, it suggests a larger energy gap between the electronic levels. Consequently, the observed transition is interpreted based on the λ_{max} value.

The reactions outlined in eqn (1) and (2) clearly shows the formation of the molybdenum blue complex, signifying the formation of a specific σ bond. This complex formation is essential for the colorimetric detection mechanism, as it allows for the visual identification of orthophosphate levels through the distinct blue coloration. The calibration curve derived shows the linear relationship between absorbance and the concentration of orthophosphate (Fig. 11(b)). The statistical
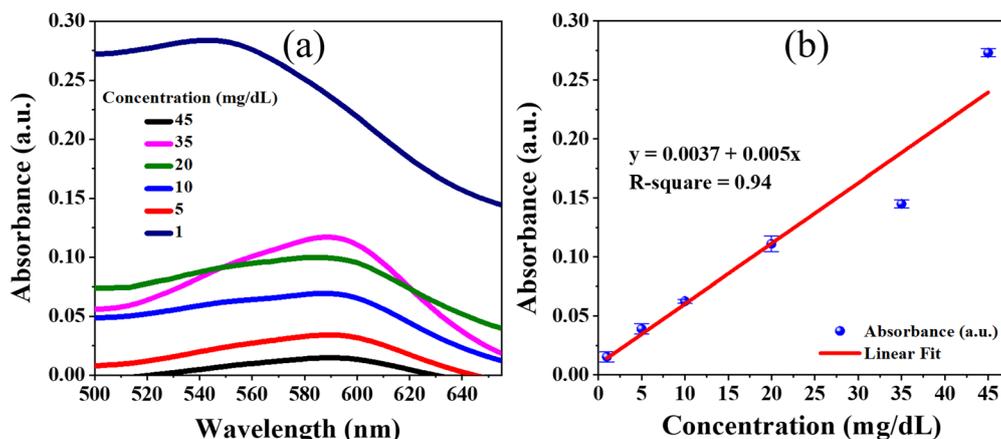

Fig. 10 (a) Absorption spectra of zincate ions with dithizone (b) linear fit curve with respect to the absorbance and concentration of zincate ions in artificial soil.
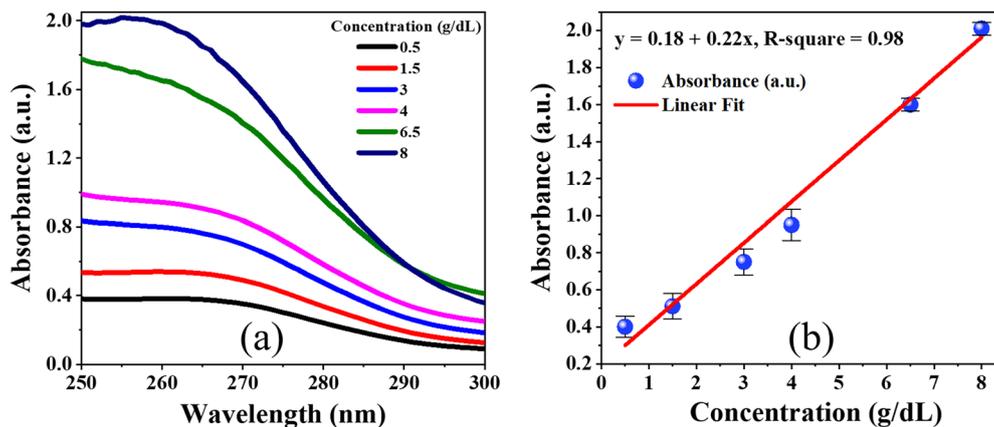
Fig. 11 (a) Absorption spectra of orthophosphate with ammonium molybdate and ascorbic acid (b) linear fit curve with respect to the absorbance and concentration of orthophosphate in artificial soil.

analysis is carried out using five repeated trials. The linear correlation observed between absorbance and concentration (g dL^{-1}) clearly indicates that higher absorbance values correspond to higher concentrations over a linear range of 0.5 g dL^{-1} to 8 g dL^{-1}.

6.3. Limit of detection (LOD)

The standard deviation (σ) is evaluated using the residual sum of squares and degree of freedom relation as mentioned in eqn (7).[43,81]

$$\sigma = \sqrt{\frac{RSS}{df}} \qquad (7)$$

The LOD is then obtained through the standard deviation using eqn (8).[81]

$$LOD = 3 \times \frac{\sigma}{\theta} \qquad (8)$$

here θ is the slope of the calibration curve.

The LOD calculated for zinc is 0.0107 g dL^{-1} with standard deviation as 0.0001 whereas for orthophosphate is 1.24 g dL^{-1} with standard deviation as 0.091.

6.4. Limit of quantification (LOQ)

The LOQ is calculated using eqn (9).[43,81]

$$LOQ = 10 \times \frac{\sigma}{\theta} \qquad (9)$$

The LOQ evaluated for zinc and orthophosphate are 0.035 g dL^{-1} and 4.1 g dL^{-1} respectively. Table 4 lists the residual sum

of square, degree of freedom, standard deviation LOD and LOQ values for the respective target analytes.

The LOD indicates the smallest concentration of an analyte that is reliably detected. On the other hand, the LOQ values signifies the lowest concentration at which the analyte is quantified with acceptable precision and accuracy. Therefore, the calculated LOD and LOQ values collectively represent the reaction's sensitivity, accuracy, and overall performance.

7. Conclusion

This research presents an innovative and efficient methodology for microfluidic colorimetric detection of soil analytes, demonstrating significant advancements in evaluating plant growth. The fabrication of microfluidic channels (µPADs) on Whatman Grade-1 paper substrate was successfully achieved using a DIY XY-Plotter and a technical drawing pen, utilizing an optimized solution of PDMS and hexane to impart the necessary hydrophobic properties for precise channel formation. The channels are formed in 15 minutes at a curing temperature of 150 °C. This study highlights the visual detection of zinc and orthophosphate over a broad range of concentrations ranging from 1–45 mg dL^{-1} and 0.5–8 g dL^{-1} respectively. The naked eye detection of zinc and orthophosphate is achieved by performing colorimetric reactions. Dithizone dissolved in methanol reacts with zincate ions to generate pink-colored metal chelate complex whereas ammonium molybdate and ascorbic acid reacts with orthophosphate to generate blue complex. The LOD values calculated for zinc and orthophosphate detection are 0.0107 g dL^{-1} and 1.24 g dL^{-1}, while LOQ values are 0.035 g dL^{-1} and 4.1 g dL^{-1} respectively. The sensitivity and selectivity of the chemical analysis provides rapid and accurate insights into the soil's nutritional composition. This method effectively addresses the limitations of traditional soil testing techniques, which are often time-consuming and labour-intensive. The integration of µPADs facilitates on-site detection, significantly reducing the time required for soil analysis and allowing for real-time decision-making in agricultural practices.

Table 4 LOD and LOQ evaluation parameters for target analytes

Compound	Residual sum of square	Degree of freedom	Standard deviation (g dL^{-1})	LOD (g dL^{-1})	LOQ
Zinc	0.00254	4	0.0001	0.0107	0.035
Orthophosphate	0.03348	4	0.091	1.24	4.1

Moreover, the cost-effectiveness and simplicity of the fabrication process make this technique accessible for widespread use, particularly in resource-limited settings. The ability to promptly and accurately assess soil micro and macronutrient levels is crucial for optimizing soil management strategies, enhancing crop productivity, and promoting sustainable agricultural practices. This research not only contributes to the advancement of soil testing methodologies but also has the potential to significantly impact agricultural productivity and environmental stewardship by providing a practical tool for soil fertility assessment and management.

Author contributions

V. V. A. directed and designed the research. P. M., P. G., P. M. and S. K. developed devices, conducted experiments, prepared Figures, collected data and did the literature survey. P. M., S. Y., S. K., S. S. and B. P. S. wrote and edited the manuscript. All authors have read and agreed to the manuscript.

Ethical approval

Not applicable. No animals or humans were used as test subjects.

Data availability

The datasets used in this study can be accessed by contacting the corresponding author.

Conflicts of interest

The authors declare no conflict of interest.

Acknowledgements

References

1 D. M. Cate, J. A. Adkins, J. Mettakoonpitak and C. S. Henry, *Anal. Chem.*, 2015, **87**, 19–41.

2 A. W. Martinez, S. T. Phillips, M. J. Butte and G. M. Whitesides, *Angew. Chem.*, 2007, **119**, 1340–1342.

3 E. Noviana, T. Ozer, C. S. Carrell, J. S. Link, C. McMahon, I. Jang and C. S. Henry, *Chem. Rev.*, 2021, **121**, 11835–11885.

4 A. W. Martinez, S. T. Phillips, B. J. Wiley, M. Gupta and G. M. Whitesides, *Lab Chip*, 2008, **8**, 2146–2150.

5 E. Carrilho, A. W. Martinez and G. M. Whitesides, *Anal. Chem.*, 2009, **81**, 7091–7095.

6 C.-K. Chiang, A. Kurniawan, C.-Y. Kao and M.-J. Wang, *Talanta*, 2019, **194**, 837–845.

7 J. Liu, X. Kong, H. Wang, Y. Zhang and Y. Fan, *Microfluid. Nanofluid.*, 2020, **24**, 6.

8 Y. He, Y. Wu, X. Xiao, J. Fu and G. Xue, *RSC Adv.*, 2014, **4**, 63860–63865.

9 S. R. Dabbagh, E. Becher, F. Ghaderinezhad, H. Havlucu, O. Ozcan, M. Ozkan, A. K. Yetisen and S. Tasoglu, *Biomicrofluidics*, 2021, **15**, 011502.

10 K. Sun, Y. Fan, M. Hebda and Y. Zhang, *Biomed. Mater. Dev.*, 2023, **1**, 388–401.

11 Y. Sameenoi, P. N. Nongkai, S. Nouanthavong, C. S. Henry and D. Nacapricha, *Analyst*, 2014, **139**, 6580–6588.

12 Y. Guan and B. Sun, *Microsyst. Nanoeng.*, 2020, **6**, 14.

13 J. Sitanurak, N. Fukana, T. Wongpakdee, Y. Thepchuay, N. Ratanawimarnwong, T. Amornsakchai and D. Nacapricha, *Talanta*, 2019, **205**, 120113.

14 J. Mettakoonpitak, K. Khongsoun, N. Wongwan, S. Kaewbutdee, A. Siripinyanond, A. Kuharuk and C. S. Henry, *Sens. Actuators, B*, 2021, **331**, 129463.

15 Y. Deng, Q. Li, Y. Zhou and J. Qian, *ACS Appl. Mater. Interfaces*, 2021, **13**, 57084–57091.

16 H. Shibata, Y. Hiruta and D. Citterio, *Analyst*, 2019, **144**, 1178–1186.

17 G. Demirel and E. Babur, *Analyst*, 2014, **139**, 2326–2331.

18 P. Kwong and M. Gupta, *Anal. Chem.*, 2012, **84**, 10129–10135.

19 Anushka, A. Bandopadhyay and P. K. Das, *Eur. Phys. J.: Spec. Top.*, 2023, **232**, 781–815.

20 J. S. Ng and M. Hashimoto, *RSC Adv.*, 2020, **10**, 29797–29807.

21 X. Tong, X. Lin, N. Duan, Z. Wang and S. Wu, *ACS Sens.*, 2022, **7**, 3947–3955.

22 P. Prabhakar, R. K. Sen, N. Dwivedi, R. Khan, P. R. Solanki, A. K. Srivastava and C. Dhand, *Front. Nanotechnol.*, 2021, **3**, 609355.

23 E. Fu and L. Wentland, *Lab Chip*, 2022, **22**, 9–25.

24 G. Aubry, H. J. Lee and H. Lu, *Anal. Chem.*, 2023, **95**, 444–467.

25 W. Alahmad, P. Varanusupakul and P. Varanusupakul, *Crit. Rev. Anal. Chem.*, 2023, **53**, 233–252.

26 R. S. Alkasir, M. Ornatska and S. Andreescu, *Anal. Chem.*, 2012, **84**, 9729–9737.

27 H. Martínez-Pérez-Cejuela, R. B. Mesquita, E. Simó-Alfonso, J. Herrero-Martínez and A. O. Rangel, *Microchim. Acta*, 2023, **190**, 126.

28 M. Y. Rashed and M. A. Hussein, *Egypt. Acad. J. Biol. Sci.*, 2023, **15**, 325–334.

29 S. B. Somvanshi, A. M. Ulloa, M. Zhao, Q. Liang, A. K. Barui, A. Lucas, K. Jadhav, J. P. Allebach and L. A. Stanciu, *Biosens. Bioelectron.*, 2022, **207**, 114214.

30 N. N. Le, H. C. T. Phan, H. K. Tran, D. M. T. Dang and C. M. Dang, *Int. J. Nanotechnol.*, 2020, **17**, 673–688.

31 A. Nilghaz, S. M. Mousavi, M. Li, J. Tian, R. Cao and X. Wang, *Trends Food Sci. Technol.*, 2021, **118**, 273–284.

32 M. Wang, J. Cui, Y. Wang, L. Yang, Z. Jia, C. Gao and H. Zhang, *J. Agric. Food Chem.*, 2022, **70**, 8188–8206.

33 M. Z. Hua and X. Lu, *ACS Sens.*, 2020, **5**, 4048–4056.

34 S. Natarajan, F. Su, J. Jayaraj, M. I. I. Shah and Y. Huang, *Analyst*, 2019, **144**, 6291–6303.

35 C. Srisomwat, A. Yakoh, N. Chuaypen, P. Tangkijvanich, T. Vilaivan and O. Chailapakul, *Anal. Chem.*, 2020, **93**, 2879–2887.

36 A. Yakoh, S. Chaiyo, W. Siangproh and O. Chailapakul, *ACS Sens.*, 2019, **4**, 1211–1221.

37 T.-T. Tsai, S.-W. Shen, C.-M. Cheng and C.-F. Chen, *Sci. Technol. Adv. Mater.*, 2013, **2**, 1345–1354.

38 D. Lin, B. Li, L. Fu, J. Qi, C. Xia, Y. Zhang, J. Chen, J. Choo and L. Chen, *Microsyst. Nanoeng.*, 2022, **8**, 53.

39 D. Lin, B. Li, J. Qi, X. Ji, S. Yang, W. Wang and L. Chen, *Sens. Actuators, B*, 2020, **303**, 127213.

40 S. Puneeth, M. Salve, R. Akshatha and S. Goel, *IEEE Trans. Device Mater. Reliab.*, 2019, **19**, 529–536.

41 S. Puneeth, N. Munigela, S. A. Puranam and S. Goel, *IEEE Trans. Electron Devices*, 2020, **67**, 2559–2565.

42 A. Zargaryan, N. Farhoudi, G. Haworth, J. F. Ashby and S. H. Au, *Sci. Rep.*, 2020, **10**, 18379.

43 P. Mishra, S. Navariya, P. Gupta, B. P. Singh, S. Chopra, S. Shrivastava and V. V. Agrawal, *R. Soc. Open Sci.*, 2024, **11**, 231168.

44 P. Mishra, P. Gupta, B. P. Singh, R. Kedia, S. Shrivastava, A. Patra, S.-J. Hwang and V. V. Agrawal, *J. Mol. Liq.*, 2024, **411**, 125707.

45 D. A. Bruzewicz, M. Reches and G. M. Whitesides, *ACS Anal. Chem.*, 2008, **80**, 3387–3392.

46 C. Gallibu, C. Gallibu, A. Avoundjian and F. A. Gomez, *Micromachines*, 2016, **7**, 6.

47 F. Ghaderinezhad, R. Amin, M. Temirel, B. Yenilmez, A. Wentworth and S. Tasoglu, *Sci. Rep.*, 2017, **7**, 3553.

48 R. Amin, F. Ghaderinezhad, C. Bridge, M. Temirel, S. Jones, P. Toloueinia and S. Tasoglu, *Anal. Chem.*, 2020, **11**, 611.

49 A. Diela, V. Pagkali, C. Kokkinos, A. Calokerinos and A. Economou, *Talanta*, 2024, **277**, 126425.

50 J. Mettakoonpitak, K. Khongsoun, N. Wongwan, S. Kaewbutdee, A. Siripinyanond, A. Kuharuk and C. S. Henry, *Sens. Actuators, B*, 2021, **331**, 129463.

51 J. L. Chen, D. I. Njoku, C. Tang, Y. Gao, J. Chen, Y. K. Peng, H. Sun, G. Mao, M. Pan and N. F. Y. Tam, *Small Methods*, 2024, 2400155.

52 R. Ghosh, S. Gopalakrishnan, R. Savitha, T. Renganathan and S. Pushpavanam, *Sci. Rep.*, 2019, **9**, 7896.

53 N. Le, H. C. Phan, D. M. Dang and C. Dang, *Appl. Biochem. Microbiol.*, 2021, **57**, 257–261.

54 P. D. Haller, C. A. Flowers and M. Gupta, *Soft Matter*, 2011, **7**, 2428–2432.

55 H. Moulahoum, *ACS Omega*, 2023, **8**, 41194–41203.

56 L. R. Sousa, L. C. Duarte and W. K. Coltro, *Sens. Actuators, B*, 2020, **312**, 128018.

57 C. Chen, H. Meng, T. Guo, S. Deshpande and H. Chen, *ACS Appl. Mater. Interfaces*, 2022, **14**, 40286–40296.

58 N. Nuchtavorn and M. Macka, *Anal. Chim. Acta*, 2016, **919**, 70–77.

59 N. N. Hamidon, Y. Hong, G. I. Salentijn and E. Verpoorte, *Anal. Chim. Acta*, 2018, **1000**, 180–190.

60 M. R. Broadley, P. J. White, J. P. Hammond, I. Zelko and A. Lux, *New Phytol.*, 2007, **173**, 677–702.

61 F. Khan, A. B. Siddique, S. Shabala, M. Zhou and C. Zhao, *Plants*, 2023, **12**, 2861.

62 M. J. Hawkesford, I. Cakmak, D. Coskun, L. J. De Kok, H. Lambers, J. K. Schjoerring and P. J. White, *Marschner's Mineral Nutrition of Plants*, Elsevier, 2023, pp. 201–281.

63 H. Lambers, *Annu. Rev. Plant Biol.*, 2022, **73**, 17–42.

64 T. S. George, P. Hinsinger and B. L. Turner, *Plant Soil*, 2016, **401**, 1–6.

65 J. Shen, L. Yuan, J. Zhang, H. Li, Z. Bai, X. Chen, W. Zhang and F. Zhang, *Plant Physiol.*, 2011, **156**, 997.

66 B. Baroowa, S. Paul and N. Gogoi, *Climate Change Agriculture: Perspectives, Sustainability Resilience*, Wiley Online Library, 2022, ch. 11, pp. 239–262.

67 J. Huang, C. Wang, L. Qi, X. Zhang, G. Tang, L. Li, J. Guo, Y. Jia, X. Dou and M. Lu, *Environ. Pollut.*, 2020, **266**, 115259.

68 M. C. Isidra-Arellano, P.-M. Delaux and O. Valdés-López, *Plant Cell Physiol.*, 2021, **62**, 392–400.

69 M. Jezek, A. C. Allan, J. J. Jones and C. M. Geilfus, *New Phytol.*, 2023, **239**, 494–505.

70 P. Rajan, R. R. Lada and M. T. MacDonald, *Am. J. Plant Sci.*, 2019, **10**, 1397.

71 A. T. Amati, *Effect of lead contaminated soils on lycopene and mineral contents of tomatoes (Solanum lycopersicum)*, Rochester Institute of Technology, 2018.

72 C. Weligama, A. Wasson, G. Permalloo and E. Delhaize, *Soil Res.*, 2022, **61**, 126–135.

73 M. Hamzah Saleem, K. Usman, M. Rizwan, H. Al Jabri and M. Alsafran, *Front. Plant Sci.*, 2022, **13**, 1033092.

74 C. R. Rice, R. A. Faulkner, R. A. Jewsbury, S. Bullock and R. Dunmore, *CrystEngComm*, 2017, **19**, 3414–3419.

75 M. M. Mentele, J. Cunningham, K. Koehler, J. Volckens and C. S. Henry, *ACS Anal. Chem.*, 2012, **84**, 4474–4480.

76 P. D. Johan, O. H. Ahmed, L. Omar and N. A. Hasbullah, *Agronomy*, 2021, **11**(10), 1–25.

77 H. Heidari-Bafroui, A. Charbaji, C. Anagnostopoulos and M. Faghri, *Sensors*, 2021, **21**, 3125.

78 S. R. Crouch and H. V. Malmstadt, *Anal. Chem.*, 1967, **39**, 1084–1089.

79 K. A. Connors, *Chemical kinetics: the study of reaction rates in solution*, Wiley-VCH Verlag GmbH, 1990.

80 M. Song, N. Adham and H. Rinderknecht, *Am. J. Clin. Pathol.*, 1976, **65**, 229–233.

81 S. Pattan, S. Jamdar, R. Godge, N. Dighe, A. Daithankar, S. Nirmal and M. Pai, *J. Chem. Pharm. Res.*, 2009, **1**, 329–335.